Supporting Information

In-Plane Optical Anisotropy of Layered Gallium Telluride

Shengxi Huang[1], Yuki Tatsumi[2], Xi Ling[1], Huaihong Guo[3], Ziqiang Wang[4], Garrett Watson[5], Alexander A. Puretzky[6], David B. Geohegan[6], Jing Kong[1], Ju Li[4], Teng Yang[2,7], Riichiro Saito[2], Mildred S. Dresselhaus[1,5*]*

[1] Department of Electrical Engineering and Computer Science, Massachusetts Institute of Technology, Cambridge, Massachusetts 02139, USA.

[2] Department of Physics, Tohoku University, Sendai, 980-8578, Japan.

[3] College of sciences, Liaoning Shihua University, Fushun, 113001, China

[4] Department of Nuclear Science and Engineering, Massachusetts Institute of Technology, Cambridge, Massachusetts 02139, USA.

[5] Department of Physics, Massachusetts Institute of Technology, Cambridge, Massachusetts 02139, USA.

[6] Center for Nanophase Materials Sciences, Oak Ridge National Laboratory, Oak Ridge, Tennessee 37831, USA.

[7] Shenyang National Laboratory for Materials Science, Institute of Metal Research, Chinese Academy of Sciences, Shenyang, 110016, China.

*** Corresponding Authors:**

Prof. Mildred S. Dresselhaus

Department of Electrical Engineering and Computer Science,

Massachusetts Institute of Technology, Cambridge, Massachusetts 02139, USA

Tel: +1-617-253-6864

Email: millie@mgm.mit.edu

Dr. Xi Ling

Department of Electrical Engineering and Computer Science,

Massachusetts Institute of Technology, Cambridge, Massachusetts 02139, USA

Tel: +1-617-253-6860

Email: xiling@mit.edu

1. Calculation of optical absorption

In order to explain the observed anisotropy of Raman scattering and optical extinction for GaTe, we carried out a calculation of the electron-photon interaction. The electron-photon matrix element, $\langle m|H_{\mathrm{op}}|i\rangle$, which can be calculated within the dipole approximation,[1] is responsible for an optical transition from the state i to m and is given by

$$\langle m|H_{\mathrm{op}}|i\rangle \propto P \cdot D_{mi} \qquad \text{(S1)}$$

where P is the polarization vector for the incident light, and D_{mi} is the dipole vector defined as $D_{mi} = \langle m|\nabla|i\rangle$. The electronic wave functions for the states i and m are obtained from first-principles density functional theory (DFT) calculations.

Optical extinction and absorption probability can be given by the absorption coefficient α, which is given by the Fermi's Golden Rule:

$$\alpha(E_L) \propto \sum_{m,i} |\langle m|H_{\mathrm{op}}|i\rangle|^2 \delta(E_m - E_i - E_L) \qquad \text{(S2)}$$

where E_L is the energy of the incident photon, and E_i (E_m) is the energy of the electronic state i (m). In the numerical calculations, we approximate the delta function $\delta(E_m - E_i - E_L)$ with a Gaussian function $\frac{1}{\sqrt{2\pi}\gamma} \exp\left\{\frac{(E_m - E_i - E_L)}{2\gamma^2}\right\}$, where γ is a broadening factor corresponding to the lifetime of a photo-excited electron. Here γ can be determined from the spectral width of the optical absorption[2] and we adopt $\gamma = 0.03$ eV in this calculation. The calculated optical absorption spectrum is shown in Figure S10(a). The absorption spectrum thus obtained reproduces the fact that ***x***- (0°) polarized light is more absorbed than ***y***- (90°) polarized light.

2. Analysis of the absorption anisotropy using group theory

Monoclinic bulk GaTe belongs to the C_{2h}^3 (*C2/m*) space group. The high symmetry points ***Γ***, ***Z*** and ***P*** in the Brillouin zone have the same C_{2h}^3 (*C2/m*) symmetry. As discussed in the main text, the direct energy bandgap occurs at the ***Z*** point and the gap energy is similar to that at the ***P*** point. Therefore we can discuss the selection rules of optical transitions near the gap energy by group theory analysis at the ***Z*** and ***P*** points in the Brillouin zone. We applied the projection operators of each irreducible representation for the C_{2h}^3 space group (Table S3) to the wave functions and determined the symmetry of

the eigenfunction for each energy band at the ***Z*** and ***P*** points. Figure 4(a) shows the selection rules of optical transitions near the Fermi energy. Details of the symmetry assignment for the energy bands are given in Figure S9. These optical transitions follow the optical selection rules of the C_{2h}^3 space group shown in Table S4. As shown in Table S4, the transitions between the A_g and B_u states and between the A_u and B_g states occur with ***x***-polarized light, while the transitions between the A_g and A_u states and between the B_g and B_u states occur with ***y***-polarized light. The main contribution near the gap energy comes from the ***x***-polarized light, and as the photon energy increases, the ***y***-polarized light is absorbed. Thus the anisotropy of the optical absorption and extinction becomes weak with increasing photon energy.

3. Analysis of Raman anisotropy using group theory

With the selection rules of optical transitions, we can explain the first-order polarization dependence presented in Table 1, Figures 2, S4, S5 and S7. The Raman intensity can be obtained by incorporating two electron-photon matrix elements with one electron-phonon matrix element as follows:[3]

$$I_v(E_L) = \left|\sum_{i,m,m'} \frac{\langle f|H_{\mathrm{op}}|m'\rangle\langle m'|H_{\mathrm{ep}}^v|m\rangle\langle m|H_{\mathrm{op}}|i\rangle}{(E_L-\Delta E_{mi})(E_L-\hbar\omega_v-\Delta E_{m'i})}\right|^2 \qquad \text{(S3)}$$

where $\Delta E_{mi} = E_m - E_i - \mathrm{i}\Gamma$, m (m') is the intermediate state and Γ is a broadening factor corresponding to the life time of the photo-excited carriers. The initial (i) and final (f) states in Eq. (S3) are the same in a Raman process. In the optical absorption and Raman spectra, finite values of the electron-photon matrix elements can be obtained when the direction of D_{mi} is not perpendicular to the light polarization direction *P* from Eq. (S1). Here, we neglect the polarization dependence of the electron-phonon matrix element $\langle m'|H_{\mathrm{ep}}^v|m\rangle$ for simplicity and thus the polarization dependence of the Raman intensity can be described by the product of two electron-photon matrix elements. We show the selection rules for the A_g and B_g Raman modes in Tables S5 and S6, respectively, and an example of the transition corresponding to the A_g and B_g modes at

the $\boldsymbol{P}$ point in Figures S10(b-c). For the A_g mode, the m and m' states have the same symmetry, and both electron-photon interaction matrices in Eq. (S3) have the same polarization dependence that gives a 180° period for the A_g polarization profile; while for the B_g mode, the m and m' states have different symmetries, and the two electron-photon interaction matrices have the opposite polarization dependences, resulting in the 90° period of the B_g polarization profiles as shown in Table 1. We can see that the calculated results well reproduce the shape of the polarization dependence of the Raman spectra found in the experiment.

4. Calculation of the interference effect

The interference effect in the sample and substrate contributes to the dependence of the observed optical extinction and Raman scattering on thickness of the sample and wavelength of the laser. We evaluate the interference effect by calculating the transmission probability with use of the transfer matrix method for the optical absorption/extinction and the enhancement factor for Raman scattering.[4–6] The refractive indices of the substrates as a function of the wavelength are adopted from Malitson, *et al.* (SiO_2)[7] and Vuye, *et al.* (Si),[8] which are listed in Table S7.

For the optical absorption of GaTe, we consider the setup of the experiment with the GaTe sample on a $d_2 = 0.5$ mm quartz substrate (Figure S11(a)) and we calculate the reflection, transmission, and absorption probabilities ($R, T,$ and A) by the transfer matrix method, as shown below. We assume the electromagnetic wave oscillating with a frequency ω and we obtain the relation between the electric and magnetic field from the Maxwell equation $\nabla \times E = -\mu_0 \frac{\partial H}{\partial t}$:

$$i\omega\mu_0 H_{i,x}(z) = -\frac{\partial E_{i,y}(z)}{\partial z} \qquad \text{(S4)}$$

where $\boldsymbol{x}$ and $\boldsymbol{y}$ are the in-plane directions, $\boldsymbol{z}$ is the direction perpendicular to the substrate layer, and μ_0 is the magnetic permeability in vacuum. The electric field in the *i*-th medium at the position of z is written as

$$E_{i,y}(z) = E_{i,+}e^{-ik_{i,z}(z-L_i)} + E_{i,-}e^{ik_{i,z}(z-L_i)} \qquad \text{(S5)}$$

where $E_{i,+}$ ($E_{i,-}$) is the amplitude of the electric field propagating in the +z (-z) direction and $L_i = \sum_{u=1}^{i-1} d_u$ in which d_u is the thickness of the u-th medium. From Eqs. (S4) and (S5), we can also obtain the expression for the magnetic field as

$$H_{i,x}(z) = -\Gamma_i\left(-E_{i,+}e^{-ik_{i,z}(z-L_i)} + E_{i,-}e^{ik_{i,z}(z-L_i)}\right) \qquad \text{(S6)}$$

where $\Gamma_i = \frac{k_{i,z}}{\omega\mu_0} = n_i\sqrt{\frac{\varepsilon_0}{\mu_0}}$. Using $E_{i,y}(L_i)$ and $H_{i,x}(L_i)$, E_+ and E_- are written as

$$E_{i,+} = \frac{1}{2}\left(E_{i,y}(L_i) + \frac{H_{i,x}(L_i)}{\Gamma_i}\right), \text{ and } E_{i,-} = \frac{1}{2}\left(E_{i,y}(L_i) - \frac{H_{i,x}(L_i)}{\Gamma_i}\right) \qquad \text{(S7)}$$

Using Eqs. (S5), (S6) and (S7), we can obtain the conditions of propagating the fields in the i-th medium ($L_i < z < L_{i+1}$) as follows:

$$\begin{pmatrix} E_{i,y}(z) \\ H_{i,x}(z) \end{pmatrix}$$

$$= \begin{pmatrix} \frac{1}{2}\left(e^{-ik_{i,z}(z-L_i)} + e^{ik_{i,z}(z-L_i)}\right) & \frac{1}{2\Gamma_i}\left(e^{-ik_{i,z}(z-L_i)} - e^{ik_{i,z}(z-L_i)}\right) \\ \frac{\Gamma_i}{2}\left(e^{-ik_{i,z}(z-L_i)} - e^{ik_{i,z}(z-L_i)}\right) & \frac{1}{2}\left(e^{-ik_{i,z}(z-L_i)} + e^{ik_{i,z}(z-L_i)}\right) \end{pmatrix} \begin{pmatrix} E_{i,y}(L_i) \\ H_{i,x}(L_i) \end{pmatrix} \qquad \text{(S8)}$$

Further, when we use the boundary conditions for $E_{i,y}$ and $H_{i,x}$ that are $E_{i,y}(L_i) = E_{i+1,y}(L_i)$ and $H_{i,x}(L_i) = H_{i+1,x}(L_i)$, the transfer matrix of the boundary conditions becomes an identity matrix. Therefore the relations of $E_{i,y}$ and $H_{i,x}$ between the depth at $z = L_i$ and $z = L_{i+1}$ are given by

$$\begin{pmatrix} E_{i,y}(L_{i+1}) \\ H_{i,x}(L_{i+1}) \end{pmatrix}$$

$$= \begin{pmatrix} \frac{1}{2}\left(e^{-ik_{i,z}(L_{i+1}-L_i)} + e^{ik_{i,z}(L_{i+1}-L_i)}\right) & \frac{1}{2\Gamma_i}\left(e^{-ik_{i,z}(L_{i+1}-L_i)} - e^{ik_{i,z}(L_{i+1}-L_i)}\right) \\ \frac{\Gamma_i}{2}\left(e^{-ik_{i,z}(L_{i+1}-L_i)} - e^{ik_{i,z}(L_{i+1}-L_i)}\right) & \frac{1}{2}\left(e^{-ik_{i,z}(L_{i+1}-L_i)} + e^{ik_{i,z}(L_{i+1}-L_i)}\right) \end{pmatrix} \begin{pmatrix} E_{i,y}(L_i) \\ H_{i,x}(L_i) \end{pmatrix}$$

$$= \mathcal{M}_i \begin{pmatrix} E_{i,y}(L_i) \\ H_{i,x}(L_i) \end{pmatrix} \qquad \text{(S9)}$$

Using the relations of Eq. (S9) repeatedly, we can obtain the relations for $E_{i,y}$ and $H_{i,x}$ between the depth at $z = 0$ and $z = L$ as follows:

$$\begin{pmatrix} E_{0,y}(0) \\ H_{0,x}(0) \end{pmatrix} = \mathcal{M}_1^{-1}\mathcal{M}_2^{-1}\begin{pmatrix} E_{3,y}(L) \\ H_{3,x}(L) \end{pmatrix}, \qquad \text{(S10)}$$

where $\mathcal{M} = \mathcal{M}_1^{-1}\mathcal{M}_2^{-1}$ is the transfer matrix. The reflection and transmission coefficients, r and t, are associated with $E_{i,+}$ and $E_{i,-}$ as follows:

$$r = \frac{E_{0,-}}{E_{0,+}}, t = \frac{E_{3,+}}{E_{0,+}} \qquad \text{(S11)}$$

Using Eq. (S11), we can obtain the expression for r and t as follows:

$$r = \frac{M_{11}\Gamma_0 + M_{12}\Gamma_0\Gamma_3 - M_{21} - M_{22}\Gamma_3}{M_{11}\Gamma_0 + M_{12}\Gamma_0\Gamma_3 + M_{21} + M_{22}\Gamma_3}, t = \frac{2\Gamma_0}{M_{11}\Gamma_0 + M_{12}\Gamma_0\Gamma_3 + M_{21} + M_{22}\Gamma_3} \qquad \text{(S12)}$$

where M_{ij} means the i,j component of the transfer matrix $\mathcal{M}_{ij}$. Finally, the reflection, transmission, and absorption probabilities ($A, R,$ and T) are given by

$$R = |r|^2, T = |t|^2, A = 1 - R - T \qquad \text{(S13)}$$

In order to calculate the absorption probability by the transfer matrix method, we need to obtain the complex refractive index of GaTe. We calculate the refractive index by a first-principles calculation, and also by fitting with the experimental extinction spectra to the Drude-Lorentz model;

$$\varepsilon' = 1 - \frac{{\omega_p}^2\left({\omega^2 - {\omega_0}^2}\right)^2}{(\omega^2 - {\omega_0}^2)^2 + (\omega/\tau)^2}, \text{ and } \varepsilon'' = \frac{{\omega_p}^2(\omega/\tau)}{(\omega^2 - {\omega_0}^2)^2 + (\omega/\tau)^2} \qquad \text{(S14)}$$

where ε' and ε'' are the real and imaginary parts of dielectric function, respectively. Here $\hbar\omega$ corresponds to the laser energy. The refractive index can be obtained by the relation:

$$n = \sqrt{\frac{\sqrt{{\varepsilon'}^2 + {\varepsilon''}^2} + \varepsilon'}{2}}, \text{ and } \kappa = \sqrt{\frac{\sqrt{{\varepsilon'}^2 + {\varepsilon''}^2} - \varepsilon'}{2}} + \frac{I}{\sqrt{2\pi}\sigma}\exp\left(-\frac{(\hbar\omega - E_0)^2}{2\sigma^2}\right). \qquad \text{(S15)}$$

We take into account the term $\frac{I}{\sqrt{2\pi}\sigma}\exp\left(-\frac{(\hbar\omega - E_0)^2}{2\sigma^2}\right)$ in κ in order to describe the absorption by the exciton. In order to reproduce the experiments, we fit with the experiments and determine the parameters: $\omega_0, \omega_p, \tau, I, \sigma,$ and E_0. We thus obtain the parameter as: $\hbar\omega_0 = 3.6$ eV, $\hbar\omega_p = 10.2$ eV, $\tau/\hbar = 2.7$ eV^{-1}, $I = 0.17$ eV, $\sigma = 0.20$ eV, and $E_0 = 1.62$ eV for $\boldsymbol{x}$- (0°) polarized light, and $\hbar\omega_0 = 3.8$ eV, $\hbar\omega_p = 11.0$ eV, $\tau/\hbar = 2.7$ eV^{-1}, $I = 0.14$ eV, $\sigma = 0.18$ eV, and $E_0 = 1.66$ eV for $\boldsymbol{y}$- (90°) polarized light. In Figure S11(b), we show the calculated optical absorption probability using the refractive index from the first-principles calculation. The absorption probability oscillates with wavelength and GaTe thickness due to the interference effect. In Figure S11(c), we show the optical extinction spectra obtained by the Drude-Lorentz model with

the above fitting parameters. In order to compare with experiment directly, we evaluate the optical extinction $\ln(T_{\text{substrate}}/T)$, where T and $T_{\text{substrate}}$ are the transmission probability of the sample with the substrate, and only the substrate, respectively. From the fitted calculation result, we conclude that the peak at 530 nm is given by an interference effect and the peak at 730 nm is given by the absorption in GaTe.

For the observation of Raman scattering, we consider the same situation with the experiment that the GaTe sample is on the Si/SiO_2 (300 nm) substrate (Figure S12(a)). The amplitude of the excitation light at the depth z from the top of sample is given by

$$F_{ex} = t_{01}\frac{\left(1 + r_{12}r_{23}e^{-2i\beta_2}\right)e^{-i\beta_z} + \left(r_{12} + r_{23}e^{-2i\beta_2}\right)e^{-2i(\beta_1-\beta_z)}}{1 + r_{12}r_{23}e^{-2i\beta_2} + (r_{12} + r_{23}e^{-2i\beta_2})r_{01}e^{-2i\beta_1}}, \qquad \text{(S16)}$$

where $t_{ij} = 2\tilde{n}_i/(\tilde{n}_i + \tilde{n}_j)$ and $r_{ij} = (\tilde{n}_i - \tilde{n}_j)/(\tilde{n}_i + \tilde{n}_j)$ are the Fresnel transmittance and reflection coefficients at the interfaces between the *i*-th and *j*-th medium with complex refractive indices $\tilde{n}_i$ and $\tilde{n}_j$. $\beta_i = 2\pi d_i\tilde{n}_i/\lambda$ and $\beta_z = 2\pi z\tilde{n}_1/\lambda$ are the phase factors with the wavelength of the incident light λ and the thickness of the *i*-th medium d_i. We obtain the complex refractive index of GaTe from the first-principles calculation. The amplitude of the Raman scattered light at the depth z in GaTe sample is given by

$$F_{sc} = t_{10}\frac{\left(1 + r_{12}r_{23}e^{-2i\beta_2}\right)e^{-i\beta_z} + \left(r_{12} + r_{23}e^{-2i\beta_2}\right)e^{-2i(\beta_1-\beta_z)}}{1 + r_{12}r_{23}e^{-2i\beta_2} + (r_{12} + r_{23}e^{-2i\beta_2})r_{01}e^{-2i\beta_1}}. \qquad \text{(S17)}$$

We can assume that β_i is the same for F_{ex} and F_{sc} since the wavenumber of the scattered light is almost the same as the incident light. Actually, the Raman shift of GaTe observed in this experiment is smaller than 300 cm^{-1}. The total enhancement factor F is written as follows:

$$F = \int_0^{d_1} |F_{ex} \cdot F_{sc}|^2 \, dz, \qquad \text{(S18)}$$

and the total Raman intensity I is written as $I = I_i \cdot F$, with the intrinsic Raman intensity denoted by I_i. In the calculation of the enhancement factor, we use the refractive index obtained from the first-principles calculation. Figures S12(b-d) are the GaTe thickness dependence of the calculated enhancement factor. As seen in Figure S12(b), which shows the calculated ratio of the enhancement factors in the ***x***- and ***y***-directions for the Raman intensity, the interference effect causes the Raman intensity in the ***x***-direction to be

smaller than in the ***y***-direction for both excitation wavelengths 532 and 633 nm, and almost the same intensity in the ***x*** and ***y***-directions for the wavelength 785 nm. These differ from the experimental observations (Table 1), suggesting that the anisotropy of the Raman intensity cannot be mainly attributed to the interference effect, but is mostly due to the anisotropy of the light-matter interactions.

5. Supporting figures and tables

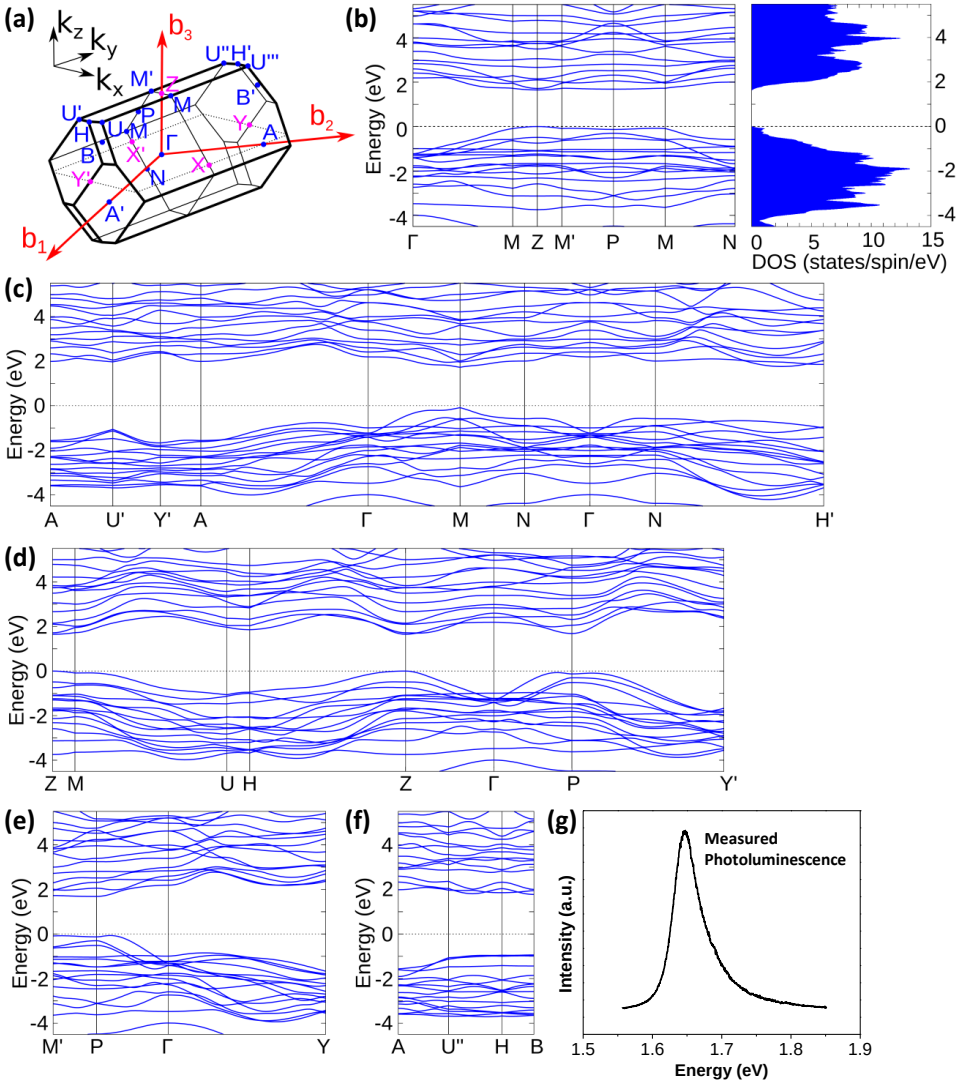

Figure S1. Electronic energy bands of bulk-GaTe. The maximum energy of the valence band at the ***Z*** point is set to zero. (a) The first Brillouin zone of GaTe showing high symmetry points. (b-f) are the energy band structures along the high-symmetry lines obtained from density functional theory (DFT) calculations. The right panel of (b) shows the density of states. (g) Measured photoluminescence spectrum of a GaTe flake with a thickness of 152 nm. The peak position is at 1.65 eV. The excitation laser wavelength is 532 nm, and the measurement was performed at room temperature. There is a direct energy bandgap at the ***Z*** point and similar bandgaps around the ***P***, ***M***, and ***M'*** points. Conduction bands are upshifted by 0.7 eV due to the underestimation of the energy gap

from the DFT calculation; thus we adjust the energy bands according to the peak position of the photoluminescence spectrum in (g).

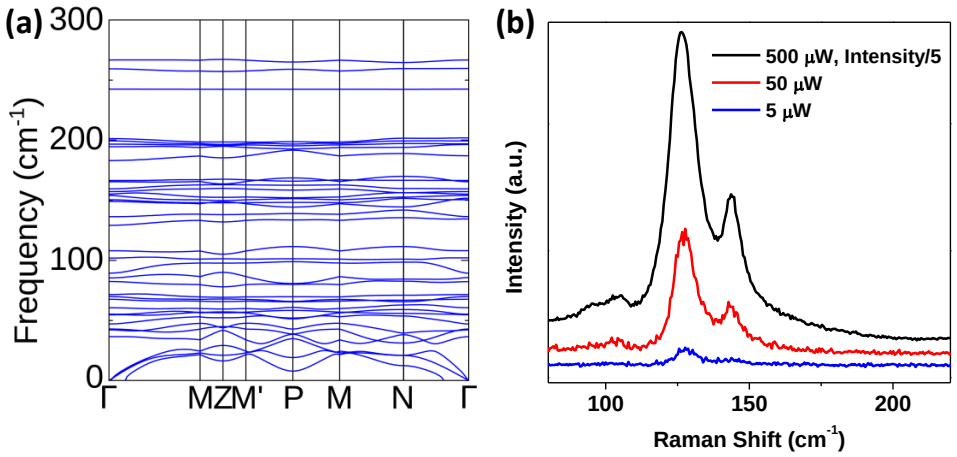

Figure S2. (a) The phonon dispersion relations of bulk GaTe along the ***Γ*–*M*–*Z*–*M'*–*P*–*M*–*N*–*Γ*** line calculated by the density functional perturbation theory (DFPT) method. From the dispersion relations, we obtained the phonon frequencies at the ***Γ*** point to assign the Raman peaks. The calculated frequency values and vibrational motions of all the phonon modes at the ***Γ*** point are listed in Table S1 and Figure S3, respectively. (b) The excitation laser power dependence of the measured Raman intensity. The Raman spectra were measured on a GaTe flake under 532 nm laser excitation with three different power levels: 500, 50 and 5 μW. The spectrum with 500 μW excitation laser power is shown with 1/5 the measured intensity. The intensities of the peaks at 126 cm^{-1} and 142 cm^{-1} are proportional to the laser power.

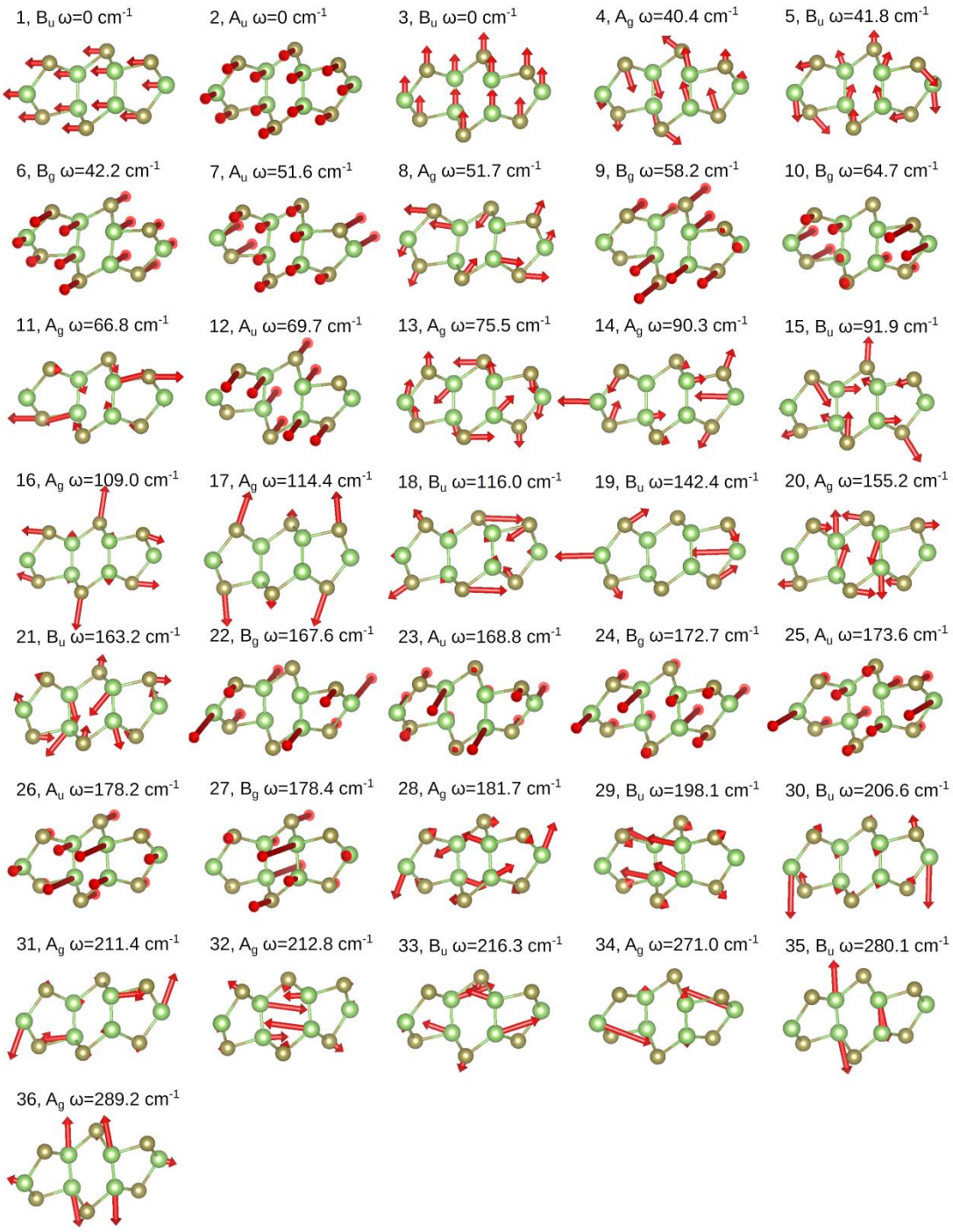

Figure S3. Illustration of the atomic vibrational motions of the phonon modes at the ***Γ*** point in bulk GaTe. See Table S1 for assignment of phonon modes.

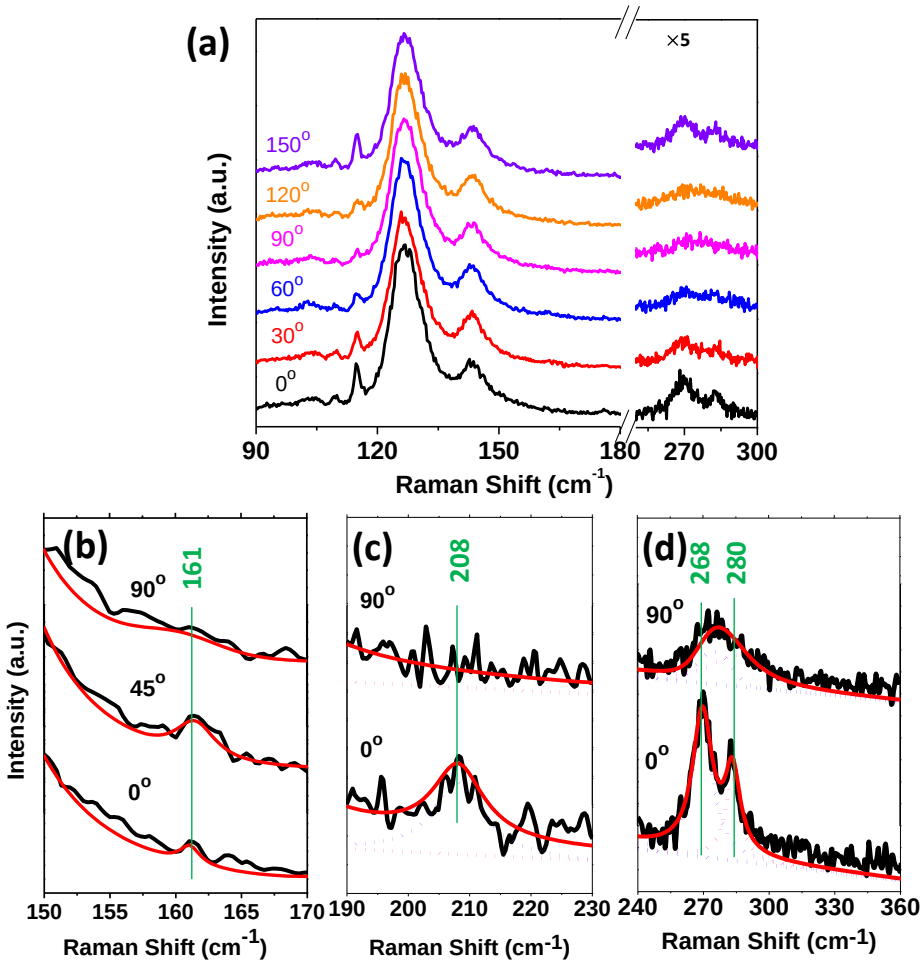

Figure S4. (a) Experimental Raman spectra of the GaTe flake in Figure 2(a) at different polarization angles from 0° to 150° with the excitation wavelength of 633 nm. (b-d) show in more detail the peak fittings and peak frequencies (in units of cm^{-1}). (b-d) show different spectral ranges.

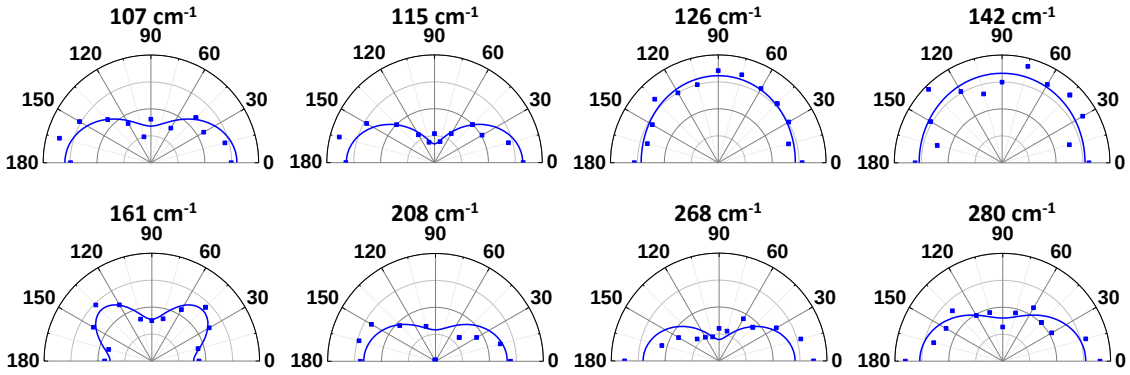

Figure S5. The Raman intensity vs. polarization angle for eight Raman modes on the same GaTe flake as shown in Figure 2. The squares are experimental values and the curves are numerical fittings. The Raman shift values are labeled above each panel. 0° (90°) corresponds to the ***x***- (***y***-) axis of the GaTe crystal.

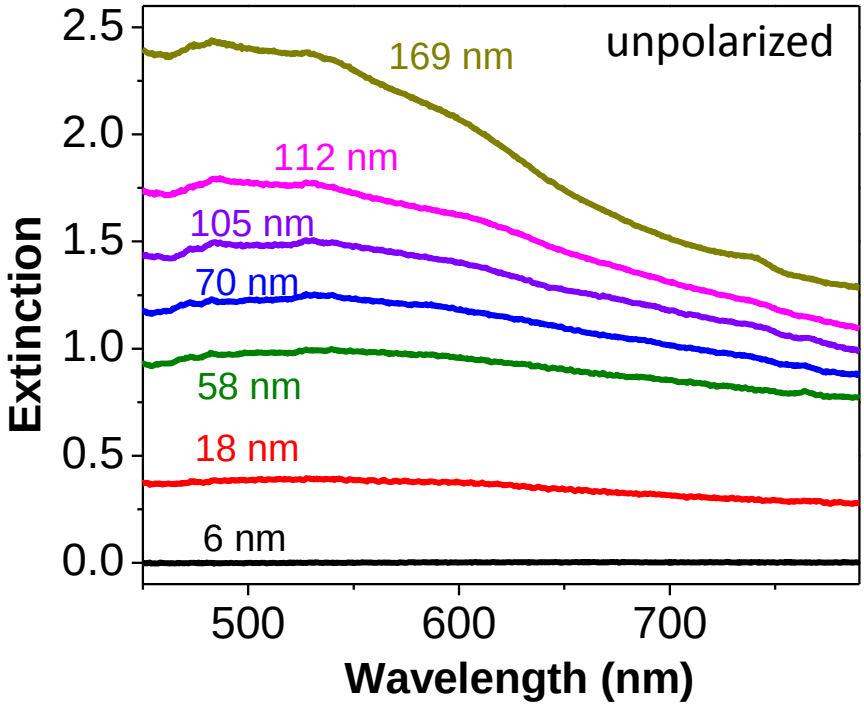

Figure S6. Non-polarized optical extinction spectra of GaTe flakes with thicknesses from 6 to 169 nm, which are labeled and color coded beside the corresponding spectra.

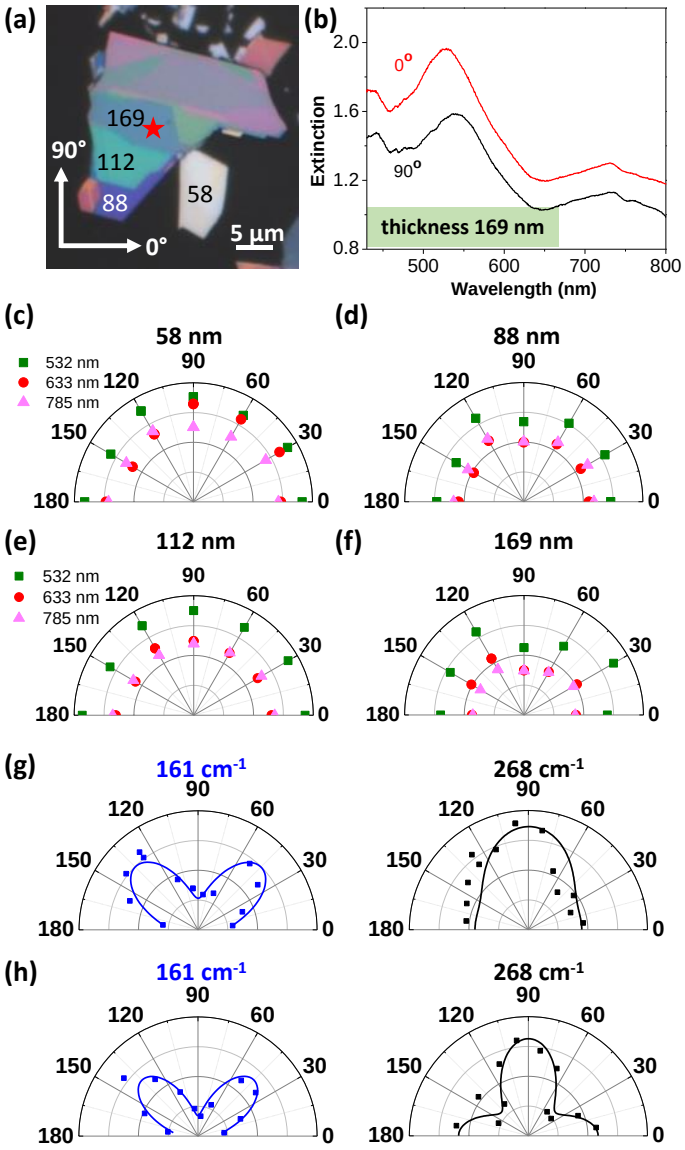

Figure S7. Polarized optical extinction and Raman spectra of GaTe. (a) The optical microscope image (same as Figure 3(a)) of the four flakes (the thicknesses are labeled in units of nm). The flakes have the same crystalline orientation, because they are physically connected to each other and are exfoliated from the same single-crystal bulk. (b) Polarized optical extinction spectra of the 169 nm-thick flake (labeled with a star in (a)) measured with incident light polarized at 0^{o} and 90^{o}. (c-f) The extinction at wavelengths 532, 633 and 785 nm with different polarization angles for flakes with thicknesses of 58, 88, 112 and 169 nm, respectively. (g-h) The polarized Raman peak intensity of the 169

nm-thick flake (g) and the 112 nm-thick flake (h) for Raman modes 161 cm^{-1} and 268 cm^{-1}. The excitation wavelength is 532 nm. The squares are experimental values and the curves are numerical fittings. The polarization angle corresponds to the angular coordinates in (a). Using the polarized Raman (g-h), we can determine that the 0° (90°) orientations in (a) and Figure 3(a) correspond to ***x***- (***y***-) axis as below. Here the excitation wavelength is 532 nm, under which the anisotropy of the 268 cm^{-1} mode with the major (secondary) maximum axis is along the ***y***- (***x***-) axis of the GaTe crystal, while the minimum values of the 161 cm^{-1} mode are along both ***x***- and ***y***-axes (Table 1). Therefore, from the polarization dependence of the Raman spectra, we can identify the crystalline orientation: for the flakes in (a) and in Figure 3 in the main text, the 0° and 90° orientations correspond to the ***x***- and ***y***-axes, respectively.

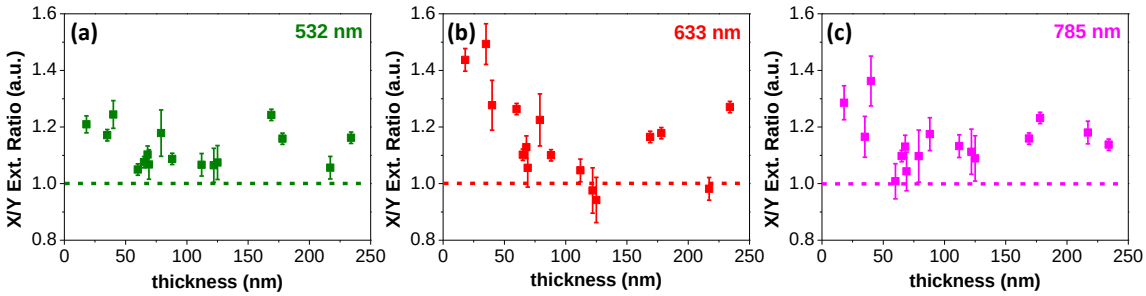

Figure S8. Thickness dependence of the extinction ratio of ***x***- and ***y***- polarized light. (a-c) show the optical extinction ratio at wavelengths 532, 633 and 785 nm, respectively. Dashed horizontal lines indicate the extinction ratio equals 1.0 (isotropic).

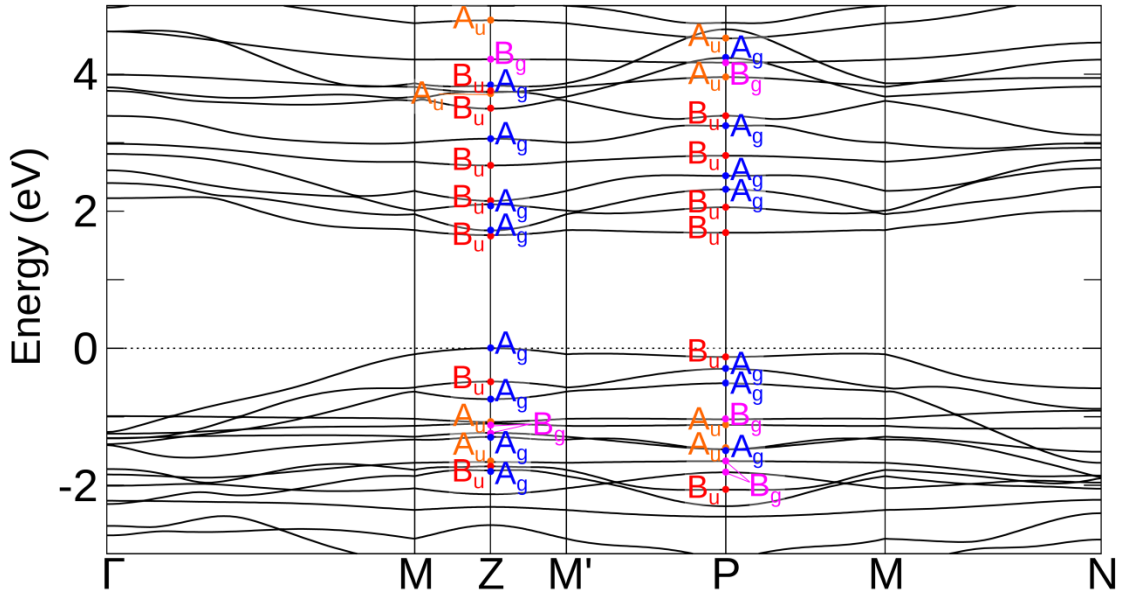

Figure S9. Symmetry assignment of the electronic energy bands of bulk GaTe at the ***Z*** and ***P*** points in the Brillouin zone. Different colors indicate different symmetries.

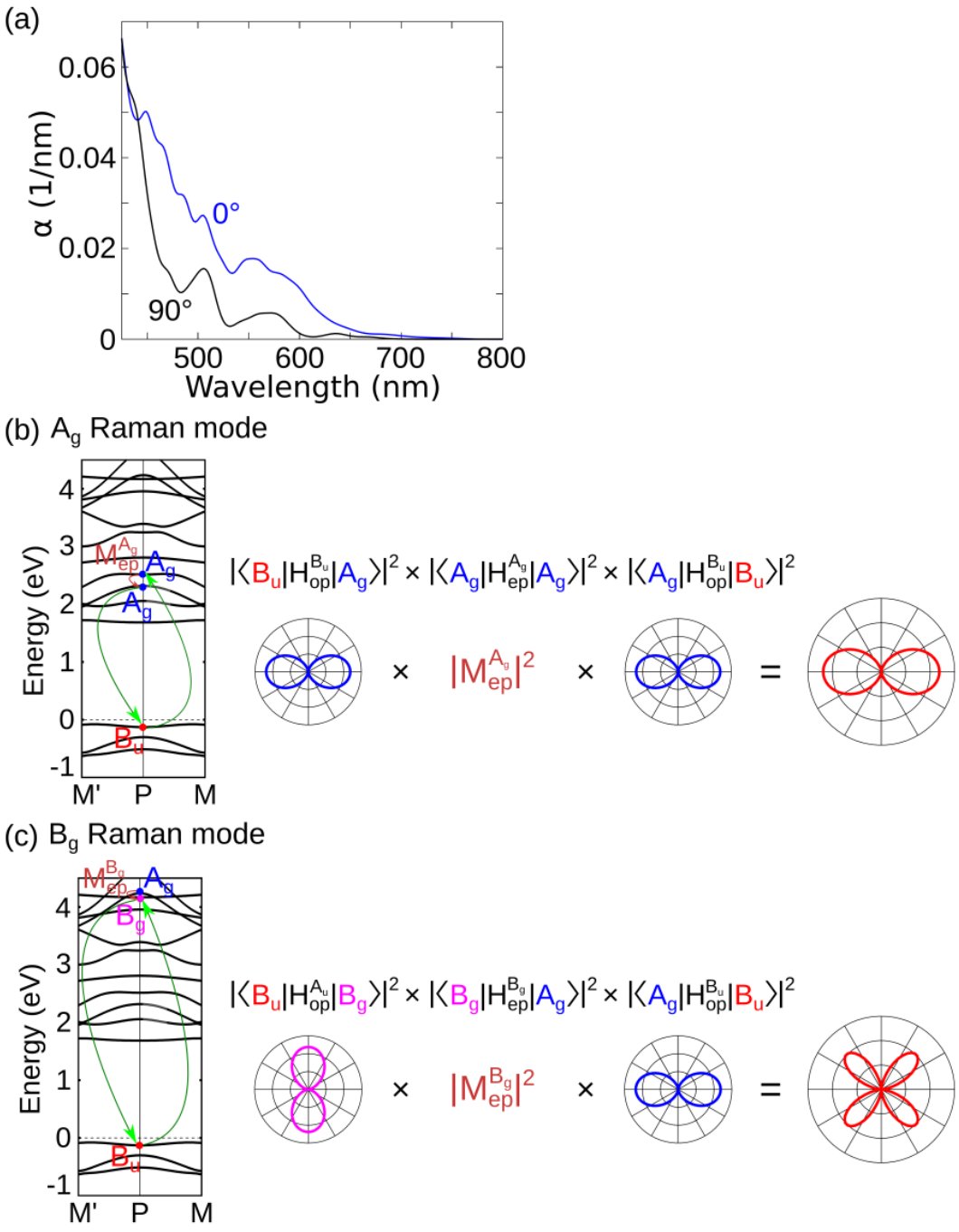

Figure S10. (a) Absorption spectrum of bulk GaTe for ***x***- (0°) and ***y***- (90°) polarized light calculated from the electron-photon matrix elements obtained by our first-principles calculation. (b-c) One of the expected transitions for Raman scattering and the expected polarization shape for the A_g (b) and B_g (c) modes at the ***P*** point. $M_{\mathrm{ep}}^{A_g}$ ($M_{\mathrm{ep}}^{B_g}$) indicates the electron-phonon interaction emitting an A_g (B_g) phonon.

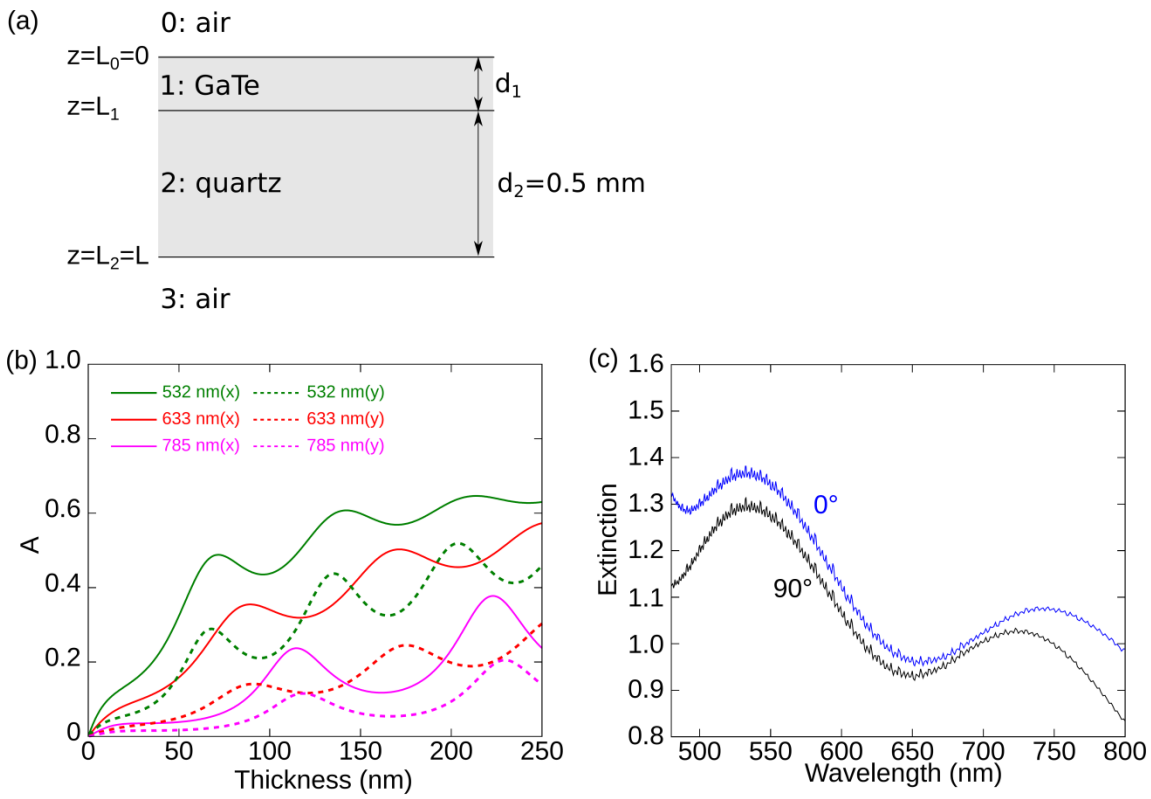

Figure S11. Calculated results for the interference effect for the optical absorption and extinction. (a) Geometrical arrangement of the experiment. (b) GaTe thickness dependence of the calculated optical absorption probability for ***x***- (solid line) and ***y***- (dashed line) polarized light. The results for the three laser energies (532, 633 and 785 nm) are shown. We use the complex refractive index obtained from the first-principles calculation (Table S7) whose energy dependence is shifted by 0.7 eV in order to be consistent with the experiment. (c) Calculated optical extinction, fitted to the experiment of the 112 nm-thick sample (Figure 3(b) in the main text) with the Drude-Lorentz model including the exciton absorption term.

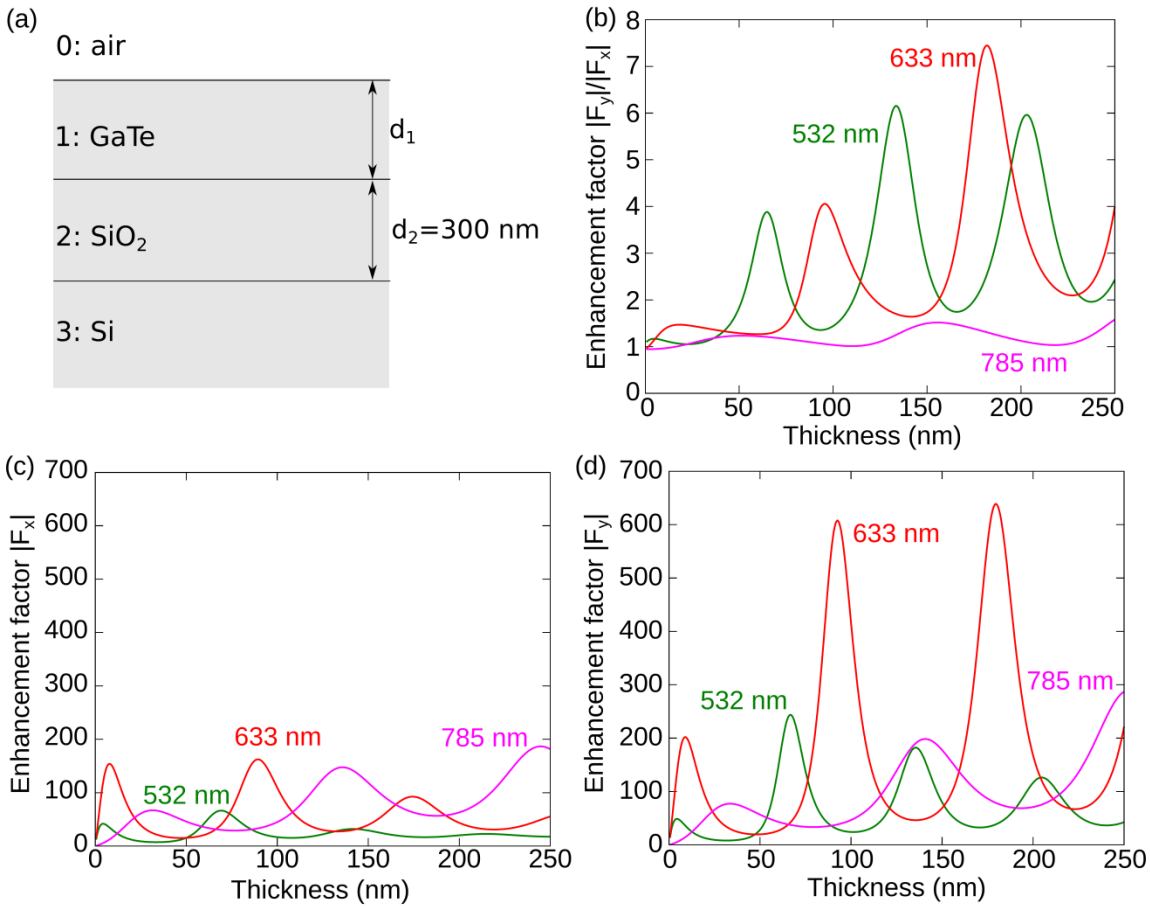

Figure S12. Calculated results for the enhancement factor for the interference effect on the Raman intensity. (a) Geometrical arrangement of the experiment. (b) The ratio of the enhancement factor for ***x***- and ***y***-polarized light as a function of GaTe thickness. (c-d) GaTe thickness dependence of the enhancement factor for ***x***- (c) and ***y***- (d) polarized light. Calculated results for the three laser wavelengths (532, 633 and 785 nm) are shown.

Table S1. Calculated Γ point phonon and assignments with experiment. Blue and red colors are Raman-active A_g and B_g modes, respectively. Black color shows the Raman-inactive modes. The labeled number of each phonon mode corresponds to the illustration in Figure S3. "Calc." and "Exp." show the calculated and experimental values of phonon frequencies, respectively.

	Calc. (cm^{-1})	Symmetry	Exp. (cm^{-1})		Calc. (cm^{-1})	Symmetry	Exp. (cm^{-1})
1	0	B_u		19	142.4	B_u	
2	0	A_u		20	155.2	A_g	
3	0	B_u		21	163.2	B_u	
4	40.4	A_g		22	167.6	B_g	161
5	41.8	B_u		23	168.8	A_u	
6	42.2	B_g		24	172.7	B_g	
7	51.6	A_u		25	173.6	A_u	
8	51.7	A_g		26	178.2	A_u	
9	58.2	B_g		27	178.4	B_g	
10	64.7	B_g		28	181.7	A_g	
11	66.8	A_g		29	198.1	B_u	
12	69.7	A_u		30	206.6	B_u	
13	75.5	A_g		31	211.4	A_g	208
14	90.3	B_u		32	212.8	A_g	208
15	91.9	B_u		33	216.3	B_u	
16	109.0	A_g	107	34	271.0	A_g	268
17	114.4	A_g	115	35	280.1	B_u	
18	116.0	B_u		36	289.2	A_g	280

Table S2. The Raman anisotropy dependence on the flake thickness and laser wavelength for the two double-resonant phonon modes: 126 and 142 cm^{-1}. The Raman intensity polar plots for the two flakes (same flakes as in Table 1) with different thicknesses: 58 and 136 nm, are shown here. These two flakes have the same crystalline orientation. The dots are experimental values and the curves are numerical fittings. The laser excitation wavelengths and the Raman peak frequencies are also labeled. 0° (90°) corresponds to the ***x***- (***y***-) axis of the GaTe crystal.

Laser / Peak (cm^{-1})	**532 nm**		**633 nm**		**785 nm**	
	Thin (58 nm)	Thick (136 nm)	Thin	Thick	Thin	Thick
126	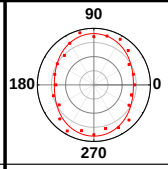	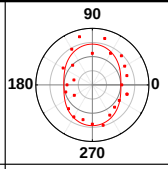	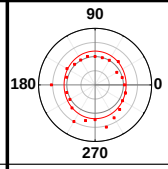	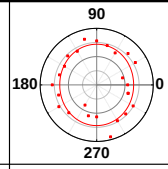	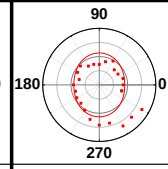	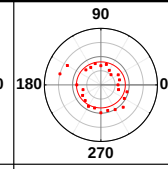
142	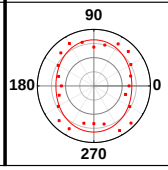	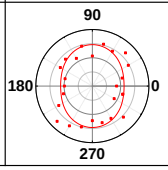	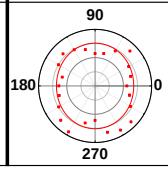	weak	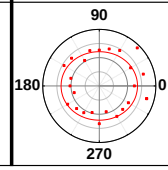	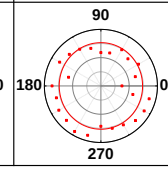

Table S3. Character table for the C_{2h}^{3} space group. $C_2(y)$ is a two-fold rotational axis along the ***y***-direction, and σ_h denotes the ***x***-***z*** mirror plane in bulk monoclinic GaTe.

C_{2h}^{3}	E	$C_2(y)$	i	σ_h	Linear functions, rotations
A_g	1	1	1	1	R_y
B_g	1	-1	1	-1	R_x, R_z
A_u	1	1	-1	-1	y
B_u	1	-1	-1	1	x, z

Table S4. Selection rules of optical transitions for the C_{2h}^{3} space group. These selection rules correspond to the electron-photon matrix element $\langle f|H_{\mathrm{op}}|i\rangle$, which is described by ∇ and is coupled by the inner product with polarization vector (Eq. (S1)).

x-polarized light $\nabla = B_u$		***y***-polarized light $\nabla = \mathrm{A}_u$	
$\|f\rangle$	$\|i\rangle$	$\|f\rangle$	$\|i\rangle$
B_u	A_g	A_u	A_g
A_u	B_g	B_u	B_g
B_g	A_u	A_g	A_u
A_g	B_u	B_g	B_u

Table S5. Selection rules of Raman scattering for the A_g mode phonon. $|i\rangle$, $|m\rangle$ and $|m'\rangle$ are the initial state and two intermediate states, respectively. ***xx*** (***yy***) are polarization vectors for the incident and scattered light: both are ***x***- (***y***-) polarized. These selection rules correspond to the product of the matrix elements: $\langle f|H_{\mathrm{op}}^{x}|m'\rangle\langle m'|H_{\mathrm{ep}}(A_g)|m\rangle\langle m|H_{\mathrm{op}}^{x}|i\rangle$ and $\langle f|H_{\mathrm{op}}^{y}|m'\rangle\langle m'|H_{\mathrm{ep}}(A_g)|m\rangle\langle m|H_{\mathrm{op}}^{y}|i\rangle$.

xx		***yy***	
$\|i\rangle = \|f\rangle$	$\|m\rangle = \|m'\rangle$	$\|i\rangle = \|f\rangle$	$\|m\rangle = \|m'\rangle$
A_g	B_u	A_g	A_u
B_g	A_u	B_g	B_u
A_u	B_g	A_u	A_g
B_u	A_g	B_u	B_g

Table S6. Selection rules of Raman scattering for the B_g mode phonon. The polarization is different for the incident and scattered light for the B_g mode. ***xy*** means that the incident light is ***y***-polarized, and the scattered light is ***x***-polarized. These selection rules correspond to the product of the matrix elements: $\langle f|H_{\mathrm{op}}^{x}|m'\rangle\langle m'|H_{\mathrm{ep}}(B_g)|m\rangle\langle m|H_{\mathrm{op}}^{y}|i\rangle$ and $\langle f|H_{\mathrm{op}}^{y}|m'\rangle\langle m'|H_{\mathrm{ep}}(B_g)|m\rangle\langle m|H_{\mathrm{op}}^{x}|i\rangle$.

xy			***yx***		
$\|i\rangle = \|f\rangle$	$\|m\rangle$	$\|m'\rangle$	$\|i\rangle = \|f\rangle$	$\|m\rangle$	$\|m'\rangle$
A_g	A_u	B_u	A_g	B_u	A_u
B_g	B_u	A_u	B_g	A_u	B_u
A_u	A_g	B_g	A_u	B_g	A_g
B_u	B_g	A_g	B_u	A_g	B_g

Table S7. Laser wavelength dependence of the complex refractive index $\tilde{n}$ of bulk GaTe for the ***x***- and ***y***- directions, SiO_2,[7] and Si.[8]

Wavelength	GaTe (***x***)	GaTe (***y***)	SiO_2	Si
532 nm	$3.70 - 0.515i$	$3.87 - 0.211i$	1.46	$4.21 - 0.010i$
633 nm	$3.74 - 0.318i$	$3.65 - 0.0926i$	1.46	$4.14 - 0.0010i$
785 nm	$3.59 - 0.0923i$	$3.49 - 0.0389i$	1.46	$4.00 - 0.0010i$

References:

(1) Sakurai, J. J.; Napolitano, J. J. *Modern Quantum Mechanics*; 2nd ed.; Addison-Wesley, 2011.

(2) Sánchez-Royo, J. F.; Segura, A.; Muñoz, V. Anisotropy of the refractive index and absorption coefficient in the layer plane of gallium telluride single crystals. *Phys. Status Solidi* **1995**, *151*, 257–265.

(3) Saito, R.; Tatsumi, Y.; Huang, S.; Ling, X.; Dresselhaus, M. S. Raman Spectroscopy of Transition Metal Dichalcogenides. *J. Phys. Condens. Matter* **2016**, *28*, 353002.

(4) Li, S.-L.; Miyazaki, H.; Song, H.; Kuramochi, H.; Nakaharai, S.; Tsukagoshi, K. Quantitative Raman Spectrum and Reliable Thickness Identification for Atomic Layers on Insulating Substrates. *ACS Nano* **2012**, *6*, 7381–7388.

(5) Yoon, D.; Moon, H.; Son, Y.-W.; Choi, J. S.; Park, B. H.; Cha, Y. H.; Kim, Y. D.; Cheong, H. Interference Effect on Raman Spectrum of Graphene on SiO2/Si. *Phys. Rev. B* **2009**, *80*, 125422.

(6) Wang, Y. Y.; Ni, Z. H.; Shen, Z. X.; Wang, H. M.; Wu, Y. H. Interference Enhancement of Raman Signal of Graphene. *Appl. Phys. Lett.* **2008**, *92*, 043121.

(7) Malitson, I. H. Interspecimen Comparison of the Refractive Index of Fused Silica. *J. Opt. Soc. Am.* **1965**, *55*, 1205.

(8) Vuye, G.; Fisson, S.; Nguyen Van, V.; Wang, Y.; Rivory, J.; Abelès, F. Temperature Dependence of the Dielectric Function of Silicon Using in Situ Spectroscopic Ellipsometry. *Thin Solid Films* **1993**, *233*, 166–170.